IEEE Access
Multidisciplinary | Rapid Review | Open Access Journal

Received May 4, 2020, accepted May 16, 2020, date of publication May 26, 2020, date of current version June 8, 2020.

Digital Object Identifier 10.1109/ACCESS.2020.2997680

Bowtie Nanoantenna Array Integrated With Artificial Impedance Surfaces for Realizing High Field Enhancement and Perfect Absorption Simultaneously

MOHAMAD KHOIRUL ANAM AND SANGJO CHOI, (Member, IEEE)
Department of Electrical Engineering, University of Ulsan, Ulsan 44610, South Korea

Corresponding author: Sangjo Choi (sangjoc@ulsan.ac.kr)

This work was supported by the National Research Foundation of Korea (NRF) Grant funded by the Korean Government (MSIT) under Grant 2020R1C1C101209911.

ABSTRACT High field enhancement and near-perfect absorption in nanoantennas were realized by using in-plane (between nanoantenna arms), out-of-plane (between nanoantenna and reflector), and array coupling (between nanoantennas in an array); however, it was challenging to satisfy both conditions at the same time. In this paper, we show that a bowtie nanoantenna array integrated with an artificial impedance surface can simultaneously satisfy both high field enhancement and perfect absorption. The artificial impedance surface is implemented as a metallic patch array on a grounded 50 nm-thick SiO_2 substrate with reactive impedance surface (RIS) or high impedance surface (HIS) characteristic. Through the proposed design methodology, we designed a bowtie nanoantenna array on an optimum RIS patch array and achieved a high field enhancement factor (E/E_0) of 228 and a nearly perfect absorption rate of 98% at 230 THz. This novel design outperforms the previously reported nanoantenna structures and the same bowtie nanoantenna array designed using a conventional grounded SiO_2. We also show that the HIS-integrated bowtie antenna array cannot realize both goals at the same time because the highly reflective HIS cannot guarantee perfect absorption. The proposed RIS-combined nanoantenna array with high field enhancement and near-perfect absorption can be used for efficient infrared (IR) and optical detectors, sensors, and energy harvesting devices.

INDEX TERMS Nanoantenna, plasmonic antenna, infrared antenna, field enhancement, absorption, artificial impedance surface, localized surface plasmon.

I. INTRODUCTION

Nanoantennas have been attracting attention as devices capable of concentrating and enhancing diffraction-limited light within subwavelength sizes and absorbing incident light efficiently [1]–[3]. Field enhancement on the nanometer scale from metallic nanoantennas is originated from the charge accumulation at the nanoantenna terminals due to localized surface plasmon resonance (LSPR) [4], [5]. The confined and enhanced fields of the nanoantenna can be used to excite fluorescent molecules and detect single molecules [6]. Additionally, with the high absorption rate, the nanoantenna can be used to improve the efficiency of infrared (IR) detectors [7], [8], plasmonic sensors [9], [10], surface-enhanced IR absorption spectroscopy [11], solar energy collection [12], and IR energy harvesting devices [13], [14].

To improve the field enhancement of the nanoantennas, researchers have been actively utilizing three methods: 1) in-plane coupling between two metallic arms of the nanoantenna [15], [16], 2) out-of-plane coupling between the nanoantenna and its image using a dielectric spacer with a metallic reflector or film [17], and 3) coupling between nanoantenna elements using nanoantenna array structures [18]–[20]. Using the grounded spacer and the array structure, optimum geometric conditions such as spacer thickness and distance between nanoantennas in the array

The associate editor coordinating the review of this manuscript and approving it for publication was Shah Nawaz Burokur.

(array pitch) to maximize the field enhancement have been studied [21]–[23]. Seok *et al*. varied the spacer thickness of a dipole nanoantenna after fixing the array pitch to 600 nm and achieved the maximum field enhancement (E/E_0) of 89 at a wavelength of 880 nm with the spacer thickness of 60 nm, which is shorter than a quarter wavelength [23]. However, the absorption rate was limited to 70% because the array pitch was not optimized for absorption improvement. Further, the optimum distance between nanoantenna elements in the array for the maximum field enhancement or absorption has been studied [24]–[28]. All of the array structures with an optimum array pitch exhibited field enhancement values (E/E_0) lower than 200 in the visible and IR range and the absorption was not perfect. Among them, the highest field enhancement value of 160 from the bowtie nanoantenna array was shown near 700 nm wavelength when the distance between the nanoantennas is 425 nm [27]. Theoretical studies also showed that the maximum field enhancement and absorption rate occur at a certain array pitch in which the scattered waves from the array and the localized surface plasmon (LSP) of each nanoantenna are coupled in-phase [29]–[31].

Furthermore, nanoantennas were designed with engineered resonant structures such as nanodisk arrays and photonic crystals (PCs) to maximize field enhancement via coupling between two different structures. Zhou *et al*. combined a bowtie nanoantenna with a hybrid nanoparticle array and provided a high field enhancement value of $\sim 2 \cdot 10^3$ at a wavelength of 750 n; however, this device was not optimized for high absorption [32]. In addition, Eter *et al*. integrated a bowtie-nanoantenna with a PC resonator and achieved a high field intensity $> 10^3$ at 1272 nm without considering perfect absorption [33]. The high field enhancement values from both cases were possible partially due to the sharp tips of the antennas in addition to the coupling.

Thus far, nanoantenna structures designed for the maximum field enhancement could not achieve perfect absorption due to dominant electric responses from the nanoantenna. For perfect absorption, a grounded ultra-thin dielectric layer can be used to induce magnetic response inside the substrate [22], [34]–[36]. A bowtie nanoantenna array backed by a grounded 5 nm-thick ($\lambda/200$) SiO_2 substrate showed perfect absorption at 1035 nm wavelength because the LSP from the nanoantenna is coupled to the ground plane. However, the field enhancement factor for this device was limited to 86 [22]. Similarly, a metal patch array with a $\lambda/150$-thick dielectric spacer showed almost perfect absorption by trapping incoming waves via the induced magnetic dipoles inside the cavity; nonetheless, this device also suffered from a low field enhancement value of 13 [34]–[36]. The reason for the low field enhancement is that the current on the nanoantenna and its image cancel each other out due to the very thin substrate. To overcome this issue, a method of simultaneously achieving perfect absorption and high field enhancement was introduced. Instead of dipole-like nanoantenna structures, triangular nanodisks were mounted on the grounded 10 nm-thick Al_2O_3 substrates, allowing for a high absorption rate of 95% and a field enhancement value of 211 at the near-IR regime [37]. The structure used an ultra-thin substrate for perfect absorption and the field enhancement was boosted by the sharp tips of the triangle shape. However, the coupling strength in such an ultra-thin substrate can be significantly affected by the surface roughness of the bottom reflector [38].

In this paper, instead of using an ultra-thin substrate with a metallic reflector, we utilized an artificial impedance surface to simultaneously fulfill the high field enhancement (> 200) and perfect absorption ($> 98\%$) of a bowtie nanoantenna array in the IR range. Here, the artificial impedance surface changes its surface impedance differently from the metallic reflector and this structure was chosen with a metallic patch array on a grounded substrate. Previously, the patch arrays have been used as the IR and optical absorbers [34], but they also have been used as a high impedance surface (HIS) and reactive impedance surface (RIS) to improve the antenna performance at microwave frequencies [39]–[43]. Because the HIS has a high surface impedance, even when the antenna is placed close to the surface, the current on the antenna and its image can be coupled in-phase. Thus, the radiation characteristic of the antenna can be improved [39], [40]. Meanwhile, the RIS can improve antenna impedance matching by offsetting the capacitive near-field characteristic of the antenna through its inductive surface impedance characteristic [41]–[43]. Recently, the RIS was utilized in a MIM (metal-insulator-metal) absorber design in the near-IR range and the structure showed the increase of field enhancement along with nearly perfect absorption due to the impedance matching between the structure and the vacuum [44]. In our study, we applied both HIS and RIS to bowtie nanoantenna design to achieve the maximum field enhancement and perfect absorption at the same time. The final bowtie nanoantenna array integrated with the optimum artificial impedance surface showed an almost perfect absorption of 98% at 230 THz ($\lambda = 1.3\ \mu$m) with a superior field enhancement factor (E/E_0) of 228. This field enhancement is ~ 1.4 times higher than the maximum value of 160 from similar nanoantenna array structures [23]–[28]. The proposed device also showed perfect absorption without the use of an ultra-thin spacer and outperformed the triangular nanodisks-based ultra-thin structure in terms of field enhancement [37]. It should be noted that a high field enhancement value (211) from the triangle-shaped structure is partially due to a very sharp tip which is not utilized in the antenna terminal (gap) of our design.

In this paper, we began with the design of a single bowtie nanoantenna on a grounded SiO_2 substrate and arranged the bowtie nanoantennas in a two-dimensional array. Then, we found the optimum pitch between the nanoantennas in the array allowing for the high field enhancement and absorption rate at 230 THz. Based on the optimum array pitch for the bowtie nanoantenna array, various metallic patch arrays for HIS and RIS were designed and integrated into the nanoantenna array. Finally, we exhibited the nanoantenna array coupled with an optimum artificial impedance surface

that realizes the maximum field enhancement and perfect absorption at the desired wavelength and also analyzed the coupling phenomena between the artificial impedance surface and the nanoantenna structure.

II. METHODS

A. NUMERICAL SIMULATION

In this study, gold and silicon dioxide (SiO_2) were used for modeling all the metallic elements and substrate material, respectively. We used the dielectric constants of SiO_2 in the near-IR region based on the previous experiments [45], [46]. The relative permittivity and conductivity of gold were calculated using the Drude model formula in (1) and (2), respectively. The angular plasma frequency (ω_p) and the carrier scattering time (τ) are $2\pi \times 2080 \times 10^{12}$ rad/s and 18 fs, respectively [47], [48].

$$\varepsilon(\omega) = 1 - \frac{\omega_p^2 \tau^2}{1 + \omega^2 \tau^2} \tag{1}$$

$$\sigma(\omega) = \frac{\varepsilon_0 \omega_p^2 \tau}{1 + \omega^2 \tau^2} \tag{2}$$

For numerical simulation, high-frequency structure simulator (HFSS) based on the finite element method (FEM) was used. In the simulations for a single bowtie nanoantenna, radiation boundaries were used for all the six surfaces of the simulation boundary box. In addition, to model an infinite bowtie nanoantenna array, we used the master and slave boundaries on the y−z and x−z planes of the simulation boundary box, and radiation boundaries were assigned on the top and bottom of the box as shown in Fig. 1. To calculate the absorption rate and field enhancement, the nanoantenna unit was illuminated with an x-polarized plane wave in a normal direction from the top. Using the reflected (P_r), transmitted (Pt), and incident (Pi) powers, the absorption rate of the nanoantenna array was determined using the equation $A = 1 - (P_r/P_i) - (P_t/P_i)$. The electric field enhancement was defined as (E/E_0), where E and E_0 are the magnitudes of the electric fields at the center of the nanoantenna gap and the incident electric field, respectively. For accurate field calculations at the nanoantenna gap, mesh sizes smaller than 1 nm were used in the nanoantenna gap region within a volume of 20 nm × 20 nm × 10 nm.

In numerical simulations for the artificial impedance surface, the PEC and PMC boundaries along the y−z and x−z planes of the simulation boundary were used to model an infinite array of metallic patches. The magnitude and phase of the reflection coefficient of the patch array were calculated using wave ports. The surface resistance and reactance of the artificial impedance surface were determined from the reflection coefficient (Γ) using the equation below

$$Z_{surface} = \frac{1 + \Gamma}{1 - \Gamma} \times Z_0 \tag{3}$$

Here, Z_0 is the characteristic impedance of the vacuum.

Meanwhile, the capacitance in the nanoantenna gap was determined with voltage gap excitation in the gap inside the radiation boundary. Then, the input reactance (X_c) was converted to the nanoantenna gap capacitance (C) using (4):

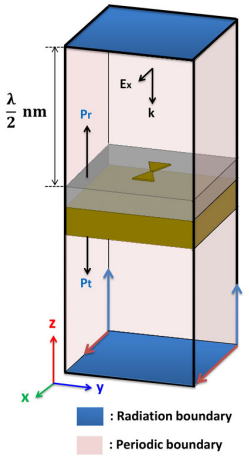

FIGURE 1. Schematic view of the nanoantenna array simulation. Master and slave boundary conditions are used along x-z and y-z planes of the simulation boundary box and radiation boundaries were assigned on the top and bottom of the box.

$$C = \frac{1}{2\pi f_{res} X_c} \tag{4}$$

B. EFFECTIVE MODE VOLUME (V_{eff}) CALCULATION

In this paper, the effective mode volume (V_{eff}) of the bowtie nanoantenna array was calculated as the ratio between the total electromagnetic energy and the peak energy density [49], [50].

$$V_{eff} = \frac{U_m}{\mu_E(r_0)} = \frac{\int \mu_E(r) d^3 r}{\mu_E(r_0)} \tag{5}$$

Here, U_m is the total electromagnetic energy inside the simulation boundary and μ_E is the electric field energy density. The simulation boundary for calculating U_m was used with the boundary of the unit cell for the nanoantenna array. Thus, r includes all the points inside the boundary. In the denominator, r_0 is the position in which energy is concentrated in the system. Here, we chose r_0 to coincide with the center of the nanoantenna gap; this was because the nanoantenna array was used to maximize the field enhancement in the nanoantenna gap. For an accurate calculation for U_m, the energy density inside the metallic structures needs to be considered due to the nonnegligible field magnitude near the metal surface. Thus, the energy density inside the metal was calculated using [51],

$$\mu_{E(metal)}(r) = \frac{1}{2}\left[\varepsilon_R + \frac{2\omega\varepsilon_I}{\gamma}\right]|E(r)|^2 \tag{6}$$

Here, $\varepsilon(\omega) = \varepsilon_R(\omega) + i\varepsilon_I(\omega)$ is the complex permittivity of the metal. ω, γ, and $E(r)$ are the angular frequency, Drude damping constant, and electric field magnitude at an arbitrary position (r), respectively. Additionally, the electric field energy density at a position, r in the dielectric medium was calculated using [52],

$$\mu_{E(dielectric)} = \frac{\varepsilon_0}{2}\varepsilon_d |E(r)|^2 \tag{7}$$

where ε_d is the dielectric constant of the medium. $\mu_E(r_0)$ was calculated using (7) because r_o is located inside the vacuum medium between the metallic nanoantenna arms.

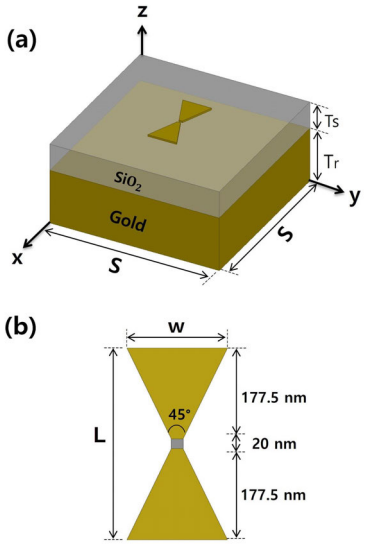

FIGURE 2. (a) Schematic view of the bowtie nanoantennas on a SiO_2 grounded substrate. The geometric values are the thickness of the SiO_2 substrate (T_s), the thickness of the gold reflector (T_r), and the size of the square SiO_2 substrate (S). (b) The detailed bowtie nanoantenna structure has a 20 nm × 20 nm × 10 nm nanoantenna gap. The dimensions of the antenna length (L) and width (w) are 375 nm and 145 nm, respectively.

III. SINGLE BOWTIE ANTENNA ON SiO_2 SUBSTRATE

A single bowtie nanoantenna was designed on a SiO_2 substrate supported by a gold reflector and its center wavelength was chosen with 1.3 μm (230 THz in frequency). The detailed design of the proposed nanoantenna is presented in Fig. 2. Here, L, w, and T_s are the nanoantenna length, width, and the SiO_2 substrate thickness, respectively. The nanoantenna air gap volume between two nanoantenna arms was fixed with 20 nm × 20 nm × 10 nm, and the thickness of the nanoantenna of 10 nm and the bowtie shape's angle of 45° were used. The substrate size (S) was set to a wavelength size (1.3 μm) such that diffraction from the edges does not change the resonant frequency of the nanoantenna. A 200 nm-thick gold reflector (T_r), which is much thicker than the metal skin depth at 230 THz, was used for proper reflection [53]. For excitation, an x-polarized plane wave with a field intensity of 1 V/m (E_0) was normally incident from above the nanoantenna and a field enhancement factor was calculated using E/E_0, where E is the electric field intensity at the center of the nanoantenna gap. With the given dimensions and excitation, we varied the nanoantenna length (L) and the SiO_2 substrate thickness (T_s) and calculated the field enhancement factor.

Field enhancement values at 230 THz as a function of the nanoantenna length (L) and SiO_2 thickness (T_s) are presented as a contour plot in Fig. 3(a). From Fig. 3(a), it can be seen that the maximum field enhancement at 230 THz is achieved when L and T_s are 375 nm and 80 nm, respectively. Electric

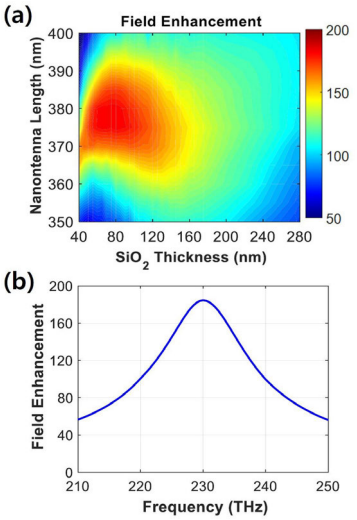

FIGURE 3. (a) The field enhancement at 230 THz with a single bowtie nanoantenna as a function of nanoantenna length (L) and SiO_2 thickness (T_s). (b) The field enhancement values versus frequency for the bowtie nanoantenna with L = 375 nm and T_s = 80 nm.

field enhancement of the corresponding bowtie nanoantenna versus frequency is shown in Fig. 3(b), showing a maximum field enhancement of 183 at 230 THz. With the 80 nm-thick SiO_2 substrates, the LSP excited by the 375 nm-long bowtie nanoantenna was optimally coupled with its image in the reflector, allowing for the maximum field enhancement at the nanoantenna gap at 230 THz. It is important to note that the thickness (80 nm) of SiO_2 for achieving the maximum field enhancement lies between a quarter-wavelength inside SiO_2 (225 nm) and an ultra-thin thickness such as 40 nm, which indicates that the radiation and absorption are balanced. This result also means that the in-phase far-field coupling between the nanoantenna and its image with a quarter-wave distance does not guarantee the maximum field enhancement in the nanoantenna gap.

IV. BOWTIE NANOANTENNA ARRAY ON SiO_2 SUBSTRATE

Using a single bowtie nanoantenna that maximizes the field enhancement at 230 THz, we designed a two-dimensional array using the master and slave boundaries and the array pitch (P) was varied to find the optimum value for the maximum field enhancement and absorption rate. The field enhancement and the absorption rate of the nanoantenna array as a function of the array pitch and frequency are presented in Figs. 4(a) and 4(b). From Figs 4(a) and 4(b), it can be observed that as the pitch increases, the electric field enhancement increases and the resonance is redshifted. The absorption rate also exhibits a redshift, but a longer pitch provides a lower absorption rate near 230 THz.

Because array pitches for the maximum field enhancement and the perfect absorption do not correspond to each other, we picked an optimum array pitch (P) of 1 μm for the balanced values in both parameters at 230 THz. One thing to note is that the optimum array pitch of 1 μm is

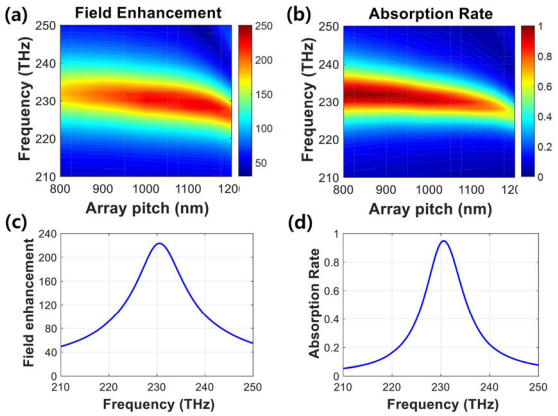

FIGURE 4. (a) The field enhancement and (b) absorption rate of the bowtie nanoantenna array on a grounded 80 nm-thick SiO_2 substrate as a function of the nanoantenna array pitch (P) and frequency. (c) The field enhancement and (d) absorption rate of the bowtie nanoantenna array with a 1 μm array pitch (P) with respect to frequency.

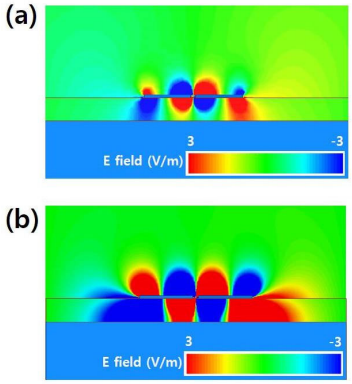

FIGURE 5. The z component of the electric field (E_z) along the antenna's central axis on the x-z plane for (a) the single bowtie nanoantenna on the grounded SiO_2 substrate with an area of 1.3 μm × 1.3 μm and (b) the bowtie nanoantenna array on the substrate with a 1 μm pitch (P). Note that an 80 nm SiO_2 thickness is used for both cases.

longer than half of the center wavelength (650 nm), which is normally used as the optimum array distance between the microwave antennas to maximize radiation at the boresight. Previous studies also showed that the optimum pitch sizes in the nanoantenna arrays occur at lengths longer than half-wavelengths [24]–[28], [54]. In the optical nanoantenna array, the in-phase coupling between the LSP from the individual nanoantenna and the scattered field from the array determined the optimum array pitch for the maximum field enhancement and absorption [22], [54].

With the optimum array pitch (P), the electric field enhancement and absorption rate of the nanoantenna array versus frequency were calculated, as shown in Figs. 4(c) and 4(d). The maximum values for the field enhancement and the absorption rate are 223 and 93%, respectively, at 230 THz. This maximum field enhancement of 223 from the bowtie nanoantenna array is higher than 184 from the single bowtie nanoantenna due to the aforementioned LSP and array resonance. It should be noted that the absorption rate is high but not perfect due to the 80 nm-thick substrate, which does not perfectly eliminate radiation loss.

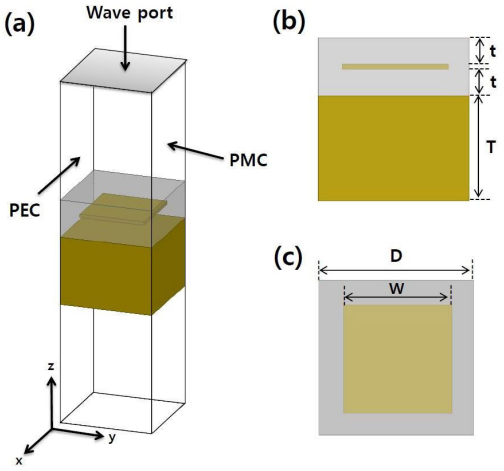

FIGURE 6. (a) Schematic view of the metallic patch unit cell with PEC and PMC boundary conditions and wave port excitation. The direction of the integration line (x-direction) in the wave port is perpendicular to the PEC boundary and is parallel to the PMC boundary. (b) Side view (y-z plane) with given dimensions of t = 50 nm and T = 200 nm. (c) Top view (x-y plane) with the patch periodicity (D) and patch width (W).

To compare the coupling between the antenna structure and the metallic reflector for both single nanoantenna and the nanoantenna array, we present the cross-sectional view of the z component of the electric field (E_z) along the antenna's central axis on the x−z plane in Fig. 5. Figs 5(a) and 5(b) effectively show that the nanoantenna array exhibits higher coupling between the antenna and the metallic reflector; this is because the LSP of the individual nanoantenna is coupled to the scattered field from the nanoantenna array [22]. In addition, higher radiation near the edges of the single nanoantenna can be seen in Fig. 5(a). Therefore, the stronger array coupling and the lower radiation resulted in higher field enhancement from the bowtie nanoantenna in the array.

V. METALLIC PATCH ARRAY DESIGN FOR HIS AND RIS

To achieve high field enhancement and perfect absorption of the bowtie nanoantenna array at the same time, we utilized the artificial impedance surface in the form of a metallic patch array on a grounded 50 nm-thick SiO_2 substrate. On top of the patch array, a 50 nm-thick SiO_2 was placed as a spacer for the nanoantenna. Then, the top surface of the SiO_2 spacer was used as a reference plane for the calculation of the reflection coefficient. The patch arrays for HIS with high resistance and RIS with high reactance were designed to achieve 0° and 90° reflection phases, respectively, in the resonant frequency of 230 THz. The detailed simulation setup for the patch array is provided in Fig. 6. The thickness of the metallic patch, the SiO_2 spacer thickness (t), and the metallic reflector thickness (T) were fixed with 10 nm, 50 nm, and 200 nm, respectively. Based on the optimum pitch (P = 1 μm) for the bowtie nanoantenna array, we chose four possible patch periodicities (D) that can be fitted inside the

1 μm $\times$ 1 μm area under the single bowtie nanoantenna. The patch periodicity values (D) were chosen as 100 nm, 125 nm, 200 nm, and 250 nm, such that 10 $\times$ 10, 8 $\times$ 8, 5 $\times$ 5, and 4 $\times$ 4 numbers of metallic patches per each periodicity can be mounted under one bowtie nanoantenna. The patch width (W) was then varied under each patch periodicity and the reflection phases along the frequency range were calculated.

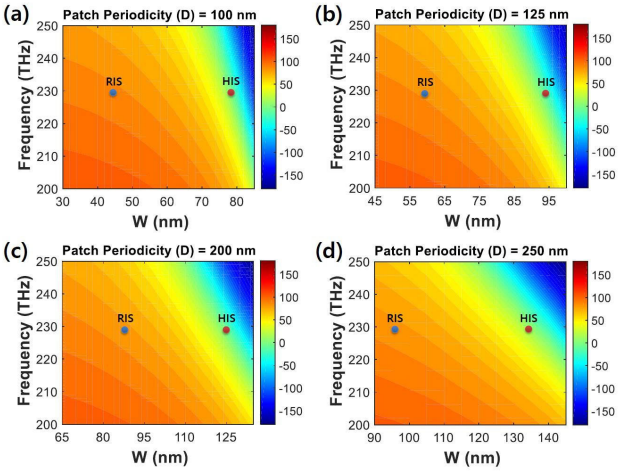

FIGURE 7. Reflection phases from the patch arrays with different patch widths (W) under the given patch periodicity (D) with (a) D = 100 nm, (b) D = 125 nm, (c) D = 200 nm, and (d) D = 250 nm. At 230 THz, the HIS and RIS parch arrays are marked by red and blue dots, respectively.

Fig. 7 shows the reflection phases of the patch arrays as a function of the patch width (W) and frequency with four different patch periodicity cases. Because of the fixed equivalent inductance via the fixed substrate thickness of the patch array, the capacitance change due to variation of the patch width resulted in a resonant frequency shift. In Fig. 7, we observe that the given patch width variation corresponds to the reflection phase shift from $-100°$ to $+100°$ at around 230 THz. Based on this, we chose specific points in which the patch arrays function as HIS and RIS using 0° and 90° reflection phases, respectively. The blue and red dots in Fig. 7 represent the points for RIS and HIS at 230 THz. A summary of the specific patch widths (W) and patch periodicities (D) for HIS and RIS is given in Table 1. In Table 1, per each periodicity (D), two different patch widths (W) for HIS and RIS are listed along with the corresponding reflection (S_{11}) phase, surface resistance (R), and surface reactance (X). The patch widths of 77.5 nm, 95 nm, 125 nm, and 135 nm show purely resistive properties with a 0° reflection phase at 230 THz, whereas the patch widths of 45 nm, 60 nm, 85 nm, and 95 nm provide inductive reactances with a 90° reflection phase at 230 THz under the patch periodicities (D) of 100 nm, 125 nm, 200 nm, and 250 nm, respectively. The table shows that the smaller patch periodicity (D) provides higher surface resistance (R) of the patch arrays for HIS, but the reactance values for RIS are maintained near 400 ohms.

TABLE 1. Summary of patch sizes and patch periodicities for the HIS and RIS at 230 THz.

D (nm)	W (nm)	S_{11} phase (°)	R (Ω)	X (Ω)	Note
100	77.5	0	6000	0	HIS
	45	90	4	383	RIS
125	95	0	5300	0	HIS
	60	90	5	405	RIS
200	125	0	4000	0	HIS
	85	90	6	427	RIS
250	135	0	3000	0	HIS
	95	90	6	421	RIS

VI. BOWTIE NANOANTENNA INTEGRATED WITH HIS AND RIS

Finally, the bowtie nanoantenna array was integrated with the patch arrays, which function as HIS or RIS and the field enhancement and the absorption rate were calculated in periodic boundary conditions. The nanoantenna structure was mounted on top of the patch array with a 50 nm-thick SiO_2 spacer and the overall area of the combined unit cell was set to 1 μm $\times$ 1 μm. Fig. 8 shows a schematic view of the integrated structure using 8 $\times$ 8 patch array for RIS with a 60 nm patch width (W) and 125 nm periodicity (D) under a single bowtie nanoantenna. Here, the nanoantenna length (L) and width (w) were slightly adjusted to 370 nm and 140 nm from 375 nm and 145 nm to maintain resonance at 230 THz for the RIS-combined nanoantenna array cases.

The field enhancement and absorption rate of the bowtie nanoantenna array combined with the HIS and RIS patch arrays are presented in Fig. 9. Overall, the nanoantennas combined with the RIS patches show higher field enhancements and absorption rates at 230 THz compared to the HIS-combined nanoantenna arrays. From Figs. 9(a) and 9(b), we find that the high surface resistance of the HIS patch arrays redshifts the resonant frequency of the nanoantenna and the maximum field enhancement values are limited at 185 near 225 THz. In detail, a HIS patch array with a smaller unit cell (W = 95 nm and D = 125 nm) supports a higher field enhancement value than that from the widest (W = 135 nm and D = 250 nm) patch. Because the HIS patch array with the shorter periodicity provides the higher surface resistance, we can understand that the nanoantenna array combined with the narrower HIS patch array provides higher field enhancement.

To understand the field distribution from the nanoantennas with the 95 nm and 135 nm-wide HIS patches, we calculated z-components of the electric fields (Ez) of both cases at 225 THz as shown in Figs. 10(a) and 10(b). Fig. 10(a) for the W = 95 nm case shows that strong fields are confined between the nanoantenna and the HIS patch array instead of the ground plane due to reflection from the HIS. We can

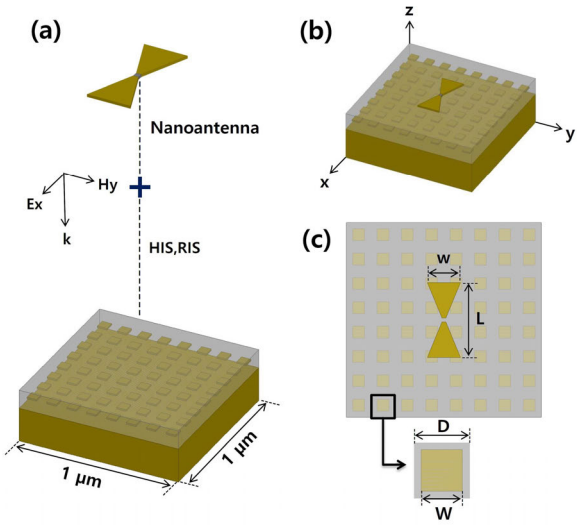

FIGURE 8. (a) Magnified view of the bowtie nanoantenna integrated with the metallic patch array. A 50 nm-thick SiO_2 spacer is used between the nanoantenna and the metallic patch array. As an example, 8 × 8 patches for the RIS with a 60 nm width (W) and 125 nm periodicity (D) are mounted under the nanoantenna, and the overall structure size is 1 μm × 1 μm. This structure is used as a unit cell with the periodic boundary and is illuminated by an x-polarized plane wave with a normal direction from the top. (b) 3D view of the integrated structure. (c) Top view of the combined structure with W = 60 nm, D = 125 nm, L = 370 nm, and w = 140 nm.

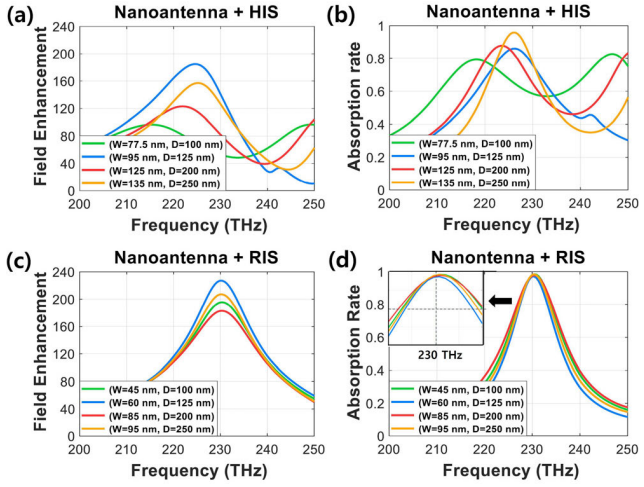

FIGURE 9. (a) Field enhancement and (b) absorption rate of the nanoantenna integrated with the HIS patch arrays. (c) Field enhancement and (d) absorption rate of the RIS-combined nanoantenna arrays. HIS and RIS patch arrays are represented by four different patch sizes (P) in each patch periodicity (D).

understand that this reflection is a reason for the higher field enhancement and the lower absorption rate for the W = 95 nm case. However, Fig. 10(b) for the 135 nm-wide HIS patch case shows that fields are distributed without significant discontinuity from the HIS and coupled to the ground similar to Fig. 5(b) for the bowtie nanoantenna array with the grounded 80 nm-thick SiO_2. This means that the coupling happens mainly between the LSP and the array diffraction, leading to a higher absorption rate of 95%, as shown in Fig. 9(b). However, the field enhancement is not increased compared

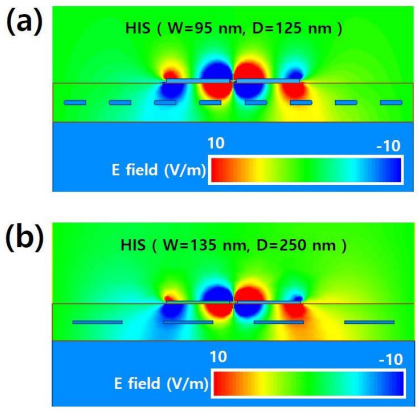

FIGURE 10. The electric field (E_z) distribution in the x−z plane of the bowtie nanoantenna combined with (a) a HIS patch (W = 95 and D = 125 nm) at 225 THz and (b) a HIS patch (W = 135 nm and D = 250 nm) at 225 THz.

to the antenna array with the 95 nm-wide HIS because the highly reflective nature from the 135 nm-wide HIS is not effective, as shown in Fig. 10(b). Overall, we found that the bowtie nanoantenna array combined with the HIS patch arrays cannot guarantee perfect absorption and high field enhancement at the same time.

In Fig. 9(c), the RIS-combined nanoantennas exhibit superior field enhancement factors higher than 180 at 230 THz. Specifically, the 60 nm-wide RIS case has the highest electric field enhancement value of 228 at 230 THz, which is higher than the value of 223 of the bowtie nanoantenna with the grounded 80 nm-thick SiO_2. In addition, as shown in Fig. 9(d), almost perfect absorption rates above 98% at 230 THz are achieved in all of the RIS case; this value is also higher than the maximum absorption rate of 93% from the bowtie nanoantenna array with the grounded SiO_2. Note that all the RIS patch array cases maintain the resonant frequencies at 230 THz, in contrast to the HIS patch array cases.

We understand that the addition of the surface inductance from the RIS underneath the capacitive bowtie nanoantenna results in almost perfect absorption of the RIS-combined structures at 230 THz. To prove the mechanism quantitatively, we calculated the capacitance of the bowtie antenna using a parallel-plate capacitor with the same size as the antenna terminal in a full-wave simulation and we found that the value was 1.71 aF. This capacitance was found to be effectively canceled by the surface inductance of 0.28 pH (equivalent to the surface reactance of 405 Ω from the 60 nm-wide RIS patch array in Table 1) at 230 THz. Therefore, we conclude that the compensation via the inductive surface impedance of the RIS patch array realizes impedance matching between the bowtie antenna array and the vacuum for the perfect absorption at 230 THz.

Fig. 9(d) (inset) shows that the 60 nm-wide RIS patch case with the highest field enhancement at 230 THz exhibits the narrowest absorption bandwidth of 5.3% (based on the full width at half maximum) versus 6.82% from the 85 nm-wide RIS patch case with the lowest field enhancement. To analyze

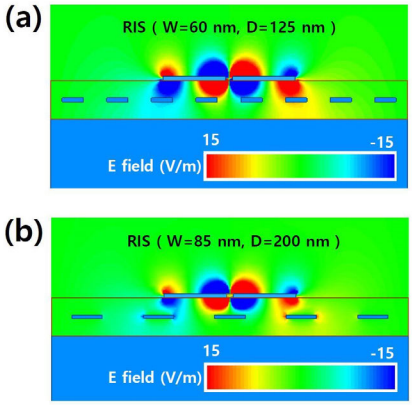

FIGURE 11. The electric field (Ez) distribution in the x−z plane with the two different RIS patch sizes: (a) Nanoantenna with a 60 nm-wide RIS patch consisting of 64 RIS patches in a 1 μm × 1 μm nanoantenna unit cell. (b) Nanoantenna with an 85 nm-wide RIS patch consisting of 25 RIS patches in a 1 μm × 1 μm nanoantenna unit cell.

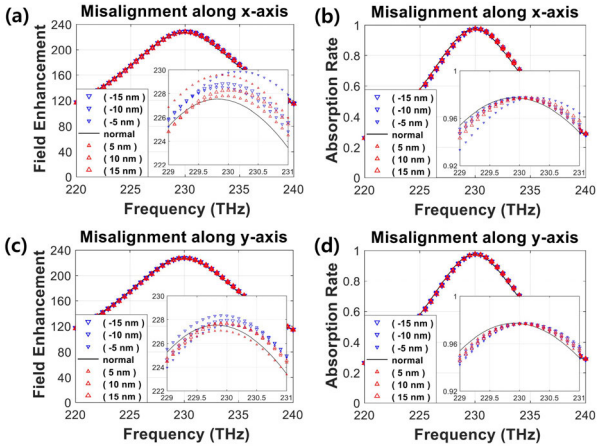

FIGURE 12. (a) Electric field enhancement and (b) absorption rate of the bowtie nanoantenna array combined with the 60 nm-wide RIS patch with the misalignment along the x-axis with −15 nm, −10 nm, −5 nm, 5 nm, 10 nm, and 15 nm from the center of the patch array. (c) Electric field enhancement and (d) absorption rate of the structure with the same misalignment along the y-axis.

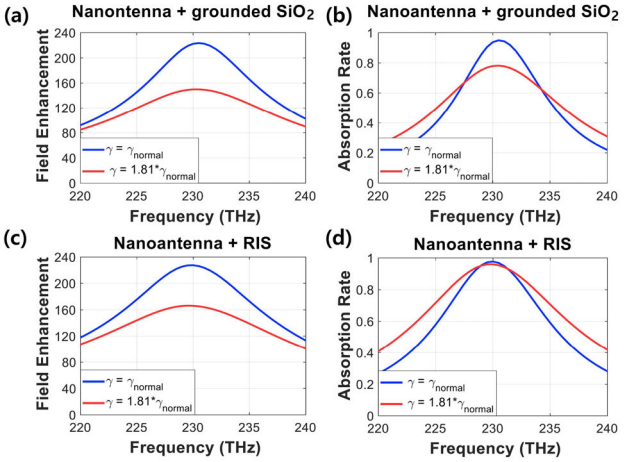

FIGURE 13. (a) Electric field enhancement and (b) absorption rate of the bowtie nanoantenna on SiO_2 grounded substrate with the different damping constants ($\gamma = \gamma_{normal}$ and $\gamma = \gamma_g = 1.81 \times \gamma_{normal}$). (c) Electric field enhancement and (d) absorption rate of the bowtie nanoantenna combined with the 60 nm-wide RIS patch with the two different damping constants.

the trade-off between the field enhancement and the bandwidth of the RIS-combined bowtie nanoantenna arrays, we calculated the Ez distribution of the 60 nm and 85 nm-wide RIS cases, as shown in Fig. 11. In the bowtie nanoantenna with the 60 nm-wide RIS patch from Fig. 11(a), a higher LSP magnitude is excited at the center of the nanoantenna and coupling between the LSP and the array diffraction is not perturbed despite the existence of the metallic patch array between the antenna and the reflector. A similar field distribution is shown in the 95 nm and 45 nm-wide RIS patch cases. However, in the 85 nm-wide RIS patch array case from Fig. 11(b), the electric fields of the nanoantenna ends are coupled to the adjacent RIS patche; thus, high electric fields are also excited at the tips of the patches. Because one of the metallic patches is located below the nanoantenna gap, the distinctive coupling occurs and causes the lowest field enhancement in the antenna gap among the RIS cases. However, the energy confinement near the patch edges contributes to the high absorption rate of the integrated structure and realizes the widest absorption bandwidth from the 85 nm-wide RIS case.

To quantify the effects of a high field excitation near the edges of the RIS patch on the field enhancement and confinement in the nanoantenna gap, we calculated the effective mode volume (V_{eff}) [23], [52]. Because the high electric field near the metallic patches for the W = 85 nm case can hinder the field concentration in the nanoantenna gap, the V_{eff} calculation based on the energy density in the nanoantenna gap is a useful parameter for comparison. From the calculation given in the Methods section, the bowtie nanoantenna with the 60 nm-wide RIS patch array shows a V_{eff} of $6.03 \times 10^{-4} \mu m^3$, whereas the 85 nm-wide RIS case maintains a higher V_{eff} of $8.38 \times 10^{-4} \mu m^3$. This higher V_{eff} from the 85 nm RIS case is correlated with the lower field enhancement at the terminal due to the excited fields near the metallic patches. Overall, the RIS-combined bowtie nanoantenna array achieved similar V_{eff} values compared to the triangle-shaped nanoantenna array [37]. Furthermore, V_{eff} can be related to the field enhancement magnitude based on the coupled-mode theory:

$$\frac{|E|^2}{|E_{inc}|^2} = A(\lambda_{res}) \frac{A_i \lambda_{res}}{\pi} \frac{Q_{abs}}{V_{eff}} \tag{8}$$

where $A(\lambda_{res})$ is the absorption rate of the nanoantenna at the resonant wavelength λ_{res}), A_i is the spot size for incident waves with a normal direction, and Q_{abs} is the absorption quality factor. From this equation, we see that a higher Q factor and a smaller V_{eff} lead to a higher electric field enhancement. Thus, a lower V_{eff} of $6.03 \times 10^{-4} \mu m^3$ and a higher Q factor of 18.85 from the 60 nm-wide RIS patch case results in a higher field enhancement compared to the 85 nm-wide RIS case with V_{eff} of 8.38×10^{-4} μm^3 and Q_{abs} of 14.64.

TABLE 2. State of the art electric field enhancement and absorption rate of the reported nanoantenna array structures.

Reference	Field enhancement (E_0/E)	Absorption rate (%)	Resonant wavelength (μm)	Nanoantenna structure in the array	Usage of lightning rod effect
Liu *et al*. 2008	80	80%	0.68	Elliptic dipole on a substrate	No
Seok *et al*. 2011	89	70%	0.88	Dipole nanoantenna on a grounded substrate	No
Zhou, *et al*. 2014	$2{\cdot}10^3$	-	0.75	Bowtie nanoantenna with a hybrid plasmonic array	Yes
Roxworthy, *et al*. 2014	160	-	0.7	Bowtie nanoantenna capped with a metallic slab	No
Eter, *et al*. 2014	$>10^3$	-	1.27	Bowtie nanoantenna with photonic crystals	Yes
Chen *et al*. 2014	126	60%	1.8	Bowtie nanoantenna with dielectric pillars	No
Lin *et al*. 2015	86	95%	1.03	Bowtie nanoantenna on a thin grounded substrate	Yes
Yong *et al*. 2016	109	98%	0.91	Circular nanodisk placed on a metallic film	No
Li *et al*. 2017	211	95%	0.9	Triangular nanodisk on a thin grounded substrate	Yes
This work	**228**	**98%**	**1.3**	**Bowtie nanoantenna with the RIS**	**No**

Furthermore, V_{eff} and Q_{abs} of the bowtie nanoantenna array on the grounded 80 nm-thick SiO_2 were calculated as 6.05×10^{-4} μm^3 and 22.54, respectively. From (8), it should be noted that the lower field enhancement from the nanoantenna array using the grounded 80 nm-thick SiO_2 compared to the 60 nm-wide RIS-combined nanoantenna array is due to the lower absorption rate, despite the similar V_{eff} and the higher Q_{abs} values.

VII. FABRICATION SENSITIVITY ANALYSIS

The performance sensitivity of the RIS-combined bowtie nanoantenna array due to the possible fabrication uncertainty was investigated. Specifically, the misalignment between the nanoantenna and the patch array, and the property change of metal from surface roughness were considered because those changes may influence near-field coupling between multiple metallic layers of the proposed structure. First, we studied the effect of the geometrical misalignment on the field enhancement and the absorption rate by moving the bowtie nanoantenna along the x-axis and y-axis with −15 nm, −10 nm, −5 nm, 5 nm, 10 nm, and 15 nm from the center of the patch array. For simulations, we chose the bowtie nanoantenna array combined with the 60 nm-wide RIS patch. Fig. 12 shows that ±15 nm misalignment results in

field enhancement change less than 1% and stable absorption rates along with a merely 0.5 THz resonant frequency shift. In detail, Figs. 12(a) and 12(c) indicate that field enhancement is relatively more sensitive to the misalignment along the x-axis instead of the y-axis because the nanoantenna is x-polarized. Figs. 12(b) and 12(d) also show the absorption rate is less sensitive than the field enhancement because the misalignment does not perturb the surface impedance of the RIS patch array. Overall, we can conclude that the proposed structure maintains a minor change in the field enhancement and absorption rate due to the misalignment between the nanoantenna and metallic patch array.

The impact on the performance due to surface roughness of the metallic structures from fabrication was also studied. Recent papers showed that the metallic nanostructures fabricated by electron beam lithography (EBL) have surface roughness near 1 nm [55], [56]. Chen *et al.* d modeled the fine roughness with 3D textures on the surface of gold nanoantennas and showed that the roughness does not change the optical property of the structures significantly in simulations [57]. On the other hand, Trugler *et a*l. measured the complex permittivity of gold before and after the annealing process and showed that gold nanostructures modeled by the measured permittivity well predict the measurement result [56]. Thus, we applied the fabrication effect on metal in numerical simulations by using the complex permittivity of metal determined by a reported grain size after the annealing process. We selected a 40 nm grain size which corresponds to surface roughness of 1.7 nm after the annealing process and calculated a damping constant of gold by [57], [58]

$$\gamma_g = \gamma_0 + \frac{1.37 V_F}{D} \frac{R}{1-R} \tag{9}$$

Here, γ_0 is a reference damping constant with infinite grain size and γ_g is the one that considers the grain size or surface roughness effect. $V_F = 1.35 \times 10^6$ m/s is the Fermi velocity of gold, D is the grain size, and R is the grain boundary reflection coefficient. From the calculation based on (9), $\gamma_g = 100.16 \times 10^{12}$ 1/s was obtained with D = 40 nm, R = 0.67, and $\gamma_0 = 6.28 \times 10^{12}$ 1/s [57]. Note that γ_g is 1.81 times larger than γ_{normal} (55×10^{12} 1/s) that was previously used for modeling gold in the bowtie nanoantenna and patch array. We converted the γ_g value to the complex permittivity via the Drude formula and applied that to all the metallic structures to consider the roughness effect. Here, the bowtie nanoantenna array on the grounded 80 nm-thick SiO_2 and the RIS-combined bowtie nanoantenna array (W = 60 nm and D = 125 nm) were simulated for comparison.

Fig. 13 compares the electric field enhancement and the absorption rate from the aforementioned two structures modeled by gold without ($\gamma = \gamma_{normal}$) and with the surface roughness effect $\gamma = \gamma_g = 1.81 \times \gamma_{normal}$). Overall, we observe that the field enhancement and the absorption are reduced with a broadened bandwidth and a slight redshift due to a higher metallic loss from the surface roughness. Among both, the bowtie nanoantenna combined with the RIS still maintains a high absorption rate of 95% and a field enhancement factor of 166 at 230 THz. These values are higher than 78% and 149 from the bowtie nanoantenna on the grounded SiO_2 spacer. Compared to the values from the case without considering the roughness effect, the RIS-combined structure shows 27% and 3% reduction in terms of the field enhancement and absorption rate; however, the counterpart suffers more with higher reduction rates, 33% and 16% for both parameters. From the simulation results, we can understand that increased metallic loss inside the patch array does not perturb its surface reactance significantly; thus, a high absorption rate from the RIS-combined nanoantenna array can be maintained. This high absorption, in turn, leads to the high field enhancement factor. From the simulation results, we conclude that the performance of the RIS-combined nanoantenna structure would be more robust than the conventional nanoantenna array even though the surface roughness effect is considered in both antenna and patch array.

VIII. CONCLUSION

We showed that the nanoantenna array combined with the RIS patch array with an optimum surface reactance could simultaneously realize high electric field enhancement (> 200) and perfect absorption (> 98%) in the IR range. Our approach overcomes the fundamental limitation of the nanoantenna array designed on an ultra-thin dielectric spacer and a reflector. First, we designed a bowtie nanoantenna array with a conventional grounded substrate and proved that the structure could not achieve both conditions at the same time due to the trade-off between two parameters. It was also shown that the nanoantenna array with the HIS patch array could not realize high absorption due to its reflective nature. Finally, the bowtie nanoantenna array designed on an optimum patch array for RIS showed a field enhancement value of 228 and a near-perfect absorption rate of 98% at 230 THz. The structure outperforms the previously reported triangle-shaped patch array designed on an ultra-thin substrate [37]. Performance comparison with the other reported nanoantennas is also provided in Table 2 and it can be found that the proposed structure shows the highest field enhancement factor among the cases with high absorption (> 90%). Note that our design achieves such a high field enhancement value without using a sharp tip for the lightning rod effect in the antenna gap that was used in the three cases with field enhancements higher than 200 in Table 2 [32], [37]. Without using a grounded ultra-thin substrate that has been used in nanoantenna design, this work showed that a nanoantenna array combined with an optimum RIS achieved high field enhancement and perfect absorption at the same time. Additional numerical simulations showed that the performance of the RIS-combined nanoantenna array was less degraded from the surface roughness effect compared to the nanoantenna array with a conventional grounded dielectric spacer. We expect that the proposed RIS-combined bowtie nanoantenna array with superior performance can be used to improve the efficiency of IR and optical detectors, plasmonic sensors, and IR energy harvesting devices.

REFERENCES

[1] L. Novotny and N. Van Hulst, "Antennas for light," *Nature Photon.*, vol. 5, no. 2, p. 83, 2011.

[2] P. Muhlschlegel, "Resonant optical antennas," *Science*, vol. 308, no. 5728, pp. 1607–1609, Jun. 2005.

[3] H. Fischer and O. J. F. Martin, "Engineering the optical response of plasmonic nanoantennas," *Opt. Express*, vol. 16, no. 12, pp. 9144–9154, 2008.

[4] A. Sundaramurthy, K. B. Crozier, G. S. Kino, D. P. Fromm, P. J. Schuck, and W. E. Moerner, "Field enhancement and gap-dependent resonance in a system of two opposing tip-to-tip au nanotriangles," *Phys. Rev. B, Condens. Matter*, vol. 72, no. 16, Oct. 2005, Art. no. 165409.

[5] E. Cubukcu, N. Yu, E. J. Smythe, L. Diehl, K. B. Crozier, and F. Capasso, "Plasmonic laser antennas and related devices," *IEEE J. Sel. Topics Quantum Electron.*, vol. 14, no. 6, pp. 1448–1461, May 2008.

[6] A. Kinkhabwala, Z. Yu, S. Fan, Y. Avlasevich, K. Müllen, and W. E. Moerner, "Large single-molecule fluorescence enhancements produced by a bowtie nanoantenna," *Nature Photon.*, vol. 3, no. 11, p. 654, 2009.

[7] L. Tang, "Nanometre-scale germanium photodetector enhanced by a near-infrared dipole antenna," *Nature Photon.*, vol. 2, no. 4, p. 226, 2008.

[8] Y. Yifat, M. Ackerman, and P. Guyot-Sionnest, "Mid-IR colloidal quantum dot detectors enhanced by optical nano-antennas," *Appl. Phys. Lett.*, vol. 110, no. 4, Jan. 2017, Art. no. 041106.

[9] N. Liu, M. Mesch, T. Weiss, M. Hentschel, and H. Giessen, "Infrared perfect absorber and its application as plasmonic sensor," *Nano Lett.*, vol. 10, no. 7, pp. 2342–2348, Jul. 2010.

[10] J. Chen, Q. Zhang, C. Peng, C. Tang, X. Shen, L. Deng, and G.-S. Park, "Optical cavity-enhanced localized surface plasmon resonance for high-quality sensing," *IEEE Photon. Technol. Lett.*, vol. 30, no. 8, pp. 728–731, Apr. 15, 2018.

[11] L. Dong, X. Yang, C. Zhang, B. Cerjan, L. Zhou, M. L. Tseng, Y. Zhang, A. Alabastri, P. Nordlander, and N. J. Halas, "Nanogapped au antennas for ultrasensitive surface-enhanced infrared absorption spectroscopy," *Nano Lett.*, vol. 17, no. 9, pp. 5768–5774, Sep. 2017.

[12] M. Gallo, L. Mescia, O. Losito, M. Bozzetti, and F. Prudenzano, "Design of optical antenna for solar energy collection," *Energy*, vol. 39, no. 1, pp. 27–32, Mar. 2012.

[13] G. Jayaswal, A. Belkadi, A. Meredov, B. Pelz, G. Moddel, and A. Shamim, "Optical rectification through an Al_2O_3 based MIM passive rectenna at 28.3 THz," *Mater. Today Energy*, vol. 7, pp. 1–9, Mar. 2018, doi: 10.1016/j.mtener.2017.11.002.

[14] B. Pelz and G. Moddel, "Demonstration of distributed capacitance compensation in a metal-insulator-metal infrared rectenna incorporating a traveling-wave diode," *J. Appl. Phys.*, vol. 125, no. 23, Jun. 2019, Art. no. 234502.

[15] S. Kim, J. Jin, Y.-J. Kim, I.-Y. Park, Y. Kim, and S.-W. Kim, "High-harmonic generation by resonant plasmon field enhancement," *Nature*, vol. 453, no. 7196, p. 757, 2008.

[16] D. P. Fromm, A. Sundaramurthy, P. J. Schuck, G. Kino, and W. E. Moerner, "Gap-dependent optical coupling of single Bowtie nanoantennas resonant in the visible," *Nano Lett.*, vol. 4, no. 5, pp. 957–961, May 2004.

[17] Y. Chu and K. B. Crozier, "Experimental study of the interaction between localized and propagating surface plasmons," *Opt. Lett.*, vol. 34, no. 3, pp. 244–246, 2009.

[18] K. Sarabandi and S. Choi, "Design optimization of bowtie nanoantenna for high-efficiency thermophotovoltaics," *J. Appl. Phys.*, vol. 114, no. 21, Dec. 2013, Art. no. 214303.

[19] S. Dodson, M. Haggui, R. Bachelot, J. Plain, S. Li, and Q. Xiong, "Optimizing electromagnetic hotspots in plasmonic bowtie nanoantennae," *J. Phys. Chem. Lett.*, vol. 4, no. 3, pp. 496–501, Feb. 2013.

[20] B. Wang, S. C. Singh, H. Lu, and C. Guo, "Design of aluminum Bowtie nanoantenna array with geometrical control to tune LSPR from UV to near-IR for optical sensing," *Plasmonics*, pp. 1–13, Nov. 2019.

[21] C. Feuillet-Palma, Y. Todorov, A. Vasanelli, and C. Sirtori, "Strong near field enhancement in THz nano-antenna arrays," *Sci. Rep.*, vol. 3, no. 1, Dec. 2013, Art. no. 1361.

[22] L. Lin and Y. Zheng, "Optimizing plasmonic nanoantennas via coordinated multiple coupling," *Sci. Rep.*, vol. 5, no. 1, Dec. 2015, Art. no. 14788.

[23] T. J. Seok, A. Jamshidi, M. Kim, S. Dhuey, A. Lakhani, H. Choo, P. J. Schuck, S. Cabrini, A. M. Schwartzberg, J. Bokor, E. Yablonovitch, and M. C. Wu, "Radiation engineering of optical antennas for maximum field enhancement," *Nano Lett.*, vol. 11, no. 7, pp. 2606–2610, Jul. 2011.

[24] L. Wang, L. Cai, J. Zhang, W. Bai, H. Hu, and G. Song, "Design of plasmonic bowtie nanoring array with high sensitivity and reproducibility for surface-enhanced Raman scattering spectroscopy," *J. Raman Spectrosc.*, vol. 42, no. 6, pp. 1263–1266, Jun. 2011.

[25] H. Chen, A. M. Bhuiya, R. Liu, D. M. Wasserman, and K. C. Toussaint, "Design, fabrication, and characterization of near-IR gold bowtie nanoantenna arrays," *J. Phys. Chem. C*, vol. 118, no. 35, pp. 20553–20558, Sep. 2014.

[26] K. D. Ko, A. Kumar, K. H. Fung, R. Ambekar, G. L. Liu, N. X. Fang, and K. C. Toussaint, "Nonlinear optical response from arrays of au bowtie nanoantennas," *Nano Lett.*, vol. 11, no. 1, pp. 61–65, Jan. 2011.

[27] B. J. Roxworthy and K. C. Toussaint, "Simultaneously tuning the electric and magnetic plasmonic response using capped bi-metallic nanoantennas," *Nanoscale*, vol. 6, no. 4, pp. 2270–2274, 2014.

[28] R. Fernández-García, Y. Sonnefraud, A. I. Fernández-Domínguez, V. Giannini, and S. A. Maier, "Design considerations for near-field enhancement in optical antennas," *Contemp. Phys.*, vol. 55, no. 1, pp. 1–11, Jan. 2014.

[29] S. Zou, N. Janel, and G. C. Schatz, "Silver nanoparticle array structures that produce remarkably narrow plasmon lineshapes," *J. Chem. Phys.*, vol. 120, no. 23, pp. 10871–10875, Jun. 2004.

[30] Y. Chu, E. Schonbrun, T. Yang, and K. B. Crozier, "Experimental observation of narrow surface plasmon resonances in gold nanoparticle arrays," *Appl. Phys. Lett.*, vol. 93, no. 18, Nov. 2008, Art. no. 181108.

[31] B. Auguié and W. L. Barnes, "Collective resonances in gold nanoparticle arrays," *Phys. Rev. Lett.*, vol. 101, no. 14, Sep. 2008, Art. no. 143902.

[32] F. Zhou, Y. Liu, and W. Cai, "Huge local electric field enhancement in hybrid plasmonic arrays," *Opt. Lett.*, vol. 39, no. 5, pp. 1302–1305, 2014.

[33] A. El Eter, T. Grosjean, P. Viktorovitch, X. Letartre, T. Benyattou, and F. I. Baida, "Huge light-enhancement by coupling a bowtie nano-antenna's plasmonic resonance to a photonic crystal mode," *Opt. Express*, vol. 22, no. 12, pp. 14464–14472, 2014.

[34] J. Hao, J. Wang, X. Liu, W. J. Padilla, L. Zhou, and M. Qiu, "High performance optical absorber based on a plasmonic metamaterial," *Appl. Phys. Lett.*, vol. 96, no. 25, Jun. 2010, Art. no. 251104.

[35] C. Wu, B. Neuner, G. Shvets, J. John, A. Milder, B. Zollars, and S. Savoy, "Large-area wide-angle spectrally selective plasmonic absorber," *Phys. Rev. B, Condens. Matter*, vol. 84, no. 7, Aug. 2011, Art. no. 075102.

[36] J. Hao, L. Zhou, and M. Qiu, "Nearly total absorption of light and heat generation by plasmonic metamaterials," *Phys. Rev. B, Condens. Matter*, vol. 83, no. 16, Apr. 2011, Art. no. 165107.

[37] Y. Li, D. Li, C. Chi, and B. Huang, "Achieving strong field enhancement and light absorption simultaneously with plasmonic nanoantennas exploiting film-coupled triangular nanodisks," *J. Phys. Chem. C*, vol. 121, no. 30, pp. 16481–16490, Aug. 2017.

[38] R. Alaee, C. Menzel, U. Huebner, E. Pshenay-Severin, S. B. Hasan, T. Pertsch, C. Rockstuhl, and F. Lederer, "Deep-subwavelength plasmonic nanoresonators exploiting extreme coupling," *Nano Lett.*, vol. 13, no. 8, pp. 3482–3486, Aug. 2013.

[39] D. Sievenpiper, L. Zhang, R. F. J. Broas, N. G. Alexopolous, and E. Yablonovitch, "High-impedance electromagnetic surfaces with a forbidden frequency band," *IEEE Trans. Microw. Theory Techn.*, vol. 47, no. 11, pp. 2059–2074, Feb. 1999.

[40] F. Yang and Y. Rahmat-Samii, "Reflection phase characterizations of the EBG ground plane for low profile wire antenna applications," *IEEE Trans. Antennas Propag.*, vol. 51, no. 10, pp. 2691–2703, Oct. 2003.

[41] H. Mosallaei and K. Sarabandi, "Antenna miniaturization and bandwidth enhancement using a reactive impedance substrate," *IEEE Trans. Antennas Propag.*, vol. 52, no. 9, pp. 2403–2414, Sep. 2004.

[42] Y. Dong, H. Toyao, and T. Itoh, "Compact circularly-polarized patch antenna loaded with metamaterial structures," *IEEE Trans. Antennas Propag.*, vol. 59, no. 11, pp. 4329–4333, 2011.

[43] S. N. Burokur, A.-C. Lepage, S. Varault, X. Begaud, G.-P. Piau, and A. de Lustrac, "Low-profile metamaterial-based L-band antennas," *Appl. Phys. A, Solids Surf.*, vol. 122, no. 4, p. 326, Apr. 2016.

[44] M. K. Anam and S. Choi, "Perfect absorption efficiency circular nanodisk array integrated with a reactive impedance surface with high field enhancement," *Nanomaterials*, vol. 10, no. 2, p. 258, Feb. 2020.

[45] I. H. Malitson, "Interspecimen comparison of the refractive index of fused silica," *J. Opt. Soc. Amer. B, Opt. Phys.*, vol. 55, no. 10, pp. 1205–1209, 1965.

[46] C. Z. Tan, "Determination of refractive index of silica glass for infrared wavelengths by IR spectroscopy," *J. Non-Crystalline Solids*, vol. 223, nos. 1–2, pp. 158–163, Jan. 1998.

[47] P. B. Johnson and R.-W. Christy, "Optical constants of the noble metals," *Phys. Rev. B, Condens. Matter*, vol. 6, no. 12, p. 4370, 1972.
[48] M. Walther, D. G. Cooke, C. Sherstan, M. Hajar, M. R. Freeman, and F. A. Hegmann, "Terahertz conductivity of thin gold films at the metal-insulator percolation transition," *Phys. Rev. B, Condens. Matter*, vol. 76, no. 12, Sep. 2007, Art. no. 125408.
[49] Y. Sonnefraud, "Experimental realization of subradiant, superradiant, and Fano resonances in ring/disk plasmonic nanocavities," *ACS nano*, vol. 4, no. 3, pp. 1664–1670, 2010.
[50] M. Decker, I. Staude, I. I. Shishkin, K. B. Samusev, P. Parkinson, V. K. A. Sreenivasan, A. Minovich, A. E. Miroshnichenko, A. Zvyagin, C. Jagadish, D. N. Neshev, and Y. S. Kivshar, "Dual-channel spontaneous emission of quantum dots in magnetic metamaterials," *Nature Commun.*, vol. 4, no. 1, p. 2949, Dec. 2013.
[51] S. A. Maier, "Plasmonic field enhancement and SERS in the effective mode volume picture," *Opt. Express*, vol. 14, no. 5, pp. 1957–1964, 2006.
[52] R. F. Oulton, V. J. Sorger, D. A. Genov, D. F. P. Pile, and X. Zhang, "A hybrid plasmonic waveguide for subwavelength confinement and long-range propagation," *Nature Photon.*, vol. 2, no. 8, p. 496, 2008.
[53] K. Arik, S. Abdollahramezani, S. Farajollahi, A. Khavasi, and B. Rejaei, "Design of mid-infrared ultra-wideband metallic absorber based on circuit theory," *Opt. Commun.*, vol. 381, pp. 309–313, Dec. 2016.
[54] B. Lee, J. Park, G. H. Han, H.-S. Ee, C. H. Naylor, W. Liu, A. T. C. Johnson, and R. Agarwal, "Fano resonance and spectrally modified photoluminescence enhancement in monolayer MoS_2 integrated with plasmonic nanoantenna array," *Nano Lett.*, vol. 15, no. 5, pp. 3646–3653, May 2015.
[55] R. Méjard, "Advanced engineering of single-crystal gold nanoantennas," *Opt. Mater. Express*, vol. 7, no. 4, pp. 1157–1168, 2017.
[56] A. Trägler, J.-C. Tinguely, G. Jakopic, U. Hohenester, J. R. Krenn, and A. Hohenau, "Near-field and SERS enhancement from rough plasmonic nanoparticles," *Phys. Rev. B, Condens. Matter*, vol. 89, no. 16, Apr. 2014, Art. no. 165409.
[57] K.-P. Chen, V. P. Drachev, J. D. Borneman, A. V. Kildishev, and V. M. Shalaev, "Drude relaxation rate in grained gold nanoantennas," *Nano Lett.*, vol. 10, no. 3, pp. 916–922, Mar. 2010, doi: 10.1021/nl9037246.
[58] A. F. Mayadas and M. Shatzkes, "Electrical-resistivity model for polycrystalline films: The case of arbitrary reflection at external surfaces," *Phys. Rev. B, Condens. Matter*, vol. 1, no. 4, p. 1382, 1970,

MOHAMAD KHOIRUL ANAM was born in Lamongan, Indonesia, in 1990. He received the B.Sc. degree in physics science from Gadjah Mada University (UGM), Indonesia, in 2013. He is currently pursuing the M.S. and Ph.D. combined degrees in electrical/electronic and computer engineering with the University of Ulsan, Ulsan, South Korea. Since 2014, he has been with the Research Center for Quality System and Testing Technology, Indonesian Institute of Sciences (LIPI). In 2017, he became a Junior Researcher and a member of the Electromagnetic Compatibility (EMC) Laboratory. His main research interests include plasmonic nanoantenna design for infrared (IR) detectors and energy harvesting devices.

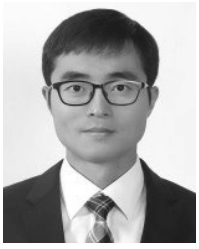

SANGJO CHOI (Member, IEEE) received the B.S. degree in electronics engineering from Kyungpook National University, Daegu, South Korea, the second B.S. degree in electrical engineering from The University of Texas at Dallas, Dallas, TX, USA, in 2008, and the M.S. and Ph.D. degrees in electrical engineering from the University of Michigan, Ann Arbor, MI, USA, in 2010 and 2014, respectively.

He was a Senior Engineer with Qualcomm Inc., San Diego, CA, USA, from 2014 to 2017. Since 2017, he has been an Assistant Professor of electrical engineering with the University of Ulsan, Ulsan, South Korea. He holds four U.S. patents. His current research interests include antennas for infrared detectors and energy harvesting devices, plasmonics, metasurfaces, band-gap structures, RF packages, and modules for wireless communications.

Dr. Choi received the Kwanjeong Scholarship form the Kwanjeong Education Foundation, South Korea, in 2008, and the Honorable Mention and was the Student Paper Competition Finalist at the IEEE International Symposium on Antenna and Propagation, in 2010 and 2013.